INORGANIC CHEMISTRY
FRONTIERS

CHINESE CHEMICAL SOCIETY
ROYAL SOCIETY OF CHEMISTRY

RESEARCH ARTICLE

View Article Online
View Journal | View Issue

Cite this: *Inorg. Chem. Front.*, 2024, **11**, 5244

Electronic metal–support interaction *via* Ni defect-induced Ru-modified Ni–CeO_2 for enhanced hydrogen oxidation activity†

Shuqing Zhou,[a] Yi Liu,[a] Lianrui Cheng,[a] Tayirjan Taylor Isimjan,*[b] Jianniao Tian *[a] and Xiulin Yang *[a]

Received 16th May 2024,
Accepted 28th June 2024

DOI: 10.1039/d4qi01233j

rsc.li/frontiers-inorganic

The creation of refined surface vacancies, a crucial bridge between theoretical structural studies and catalyst design, has attracted significant attention. Herein, we utilize a MOF pyrolytic derivatization strategy to create monodispersed Ru nanoparticles anchored on Ni–CeO_2 mesoporous microspheres with abundant Ni vacancies (Ru/Ni–CeO_2). Introducing nickel vacancies in Ru/Ni–CeO_2 is conducive to enhancing electrical conductivity and accelerating mass-charge transfer efficiency. As anticipated, the Ru/Ni–CeO_2 displays admirable hydrogen oxidation reaction (HOR) electrocatalytic activity with exchange current density (j_0) and mass activity reaching 3.27 mA cm^{-2} and 1.93 mA $g_{Ru}{}^{-1}$, respectively, surpassing the values for cutting-edge Pt/C and most recorded Ru-based HOR electrocatalysts. Surprisingly, Ru/Ni–CeO_2 demonstrates robust tolerance to 1000 ppm CO, outperforming Pt/C. Integrated analysis suggests that Ni defect-induced directional electron transfer at the Ru/Ni–CeO_2 heterointerface arises from a strong electron–metal support interaction (EMSI) effect between Ru and Ni–CeO_2. This interaction optimizes the adsorption of H and OH, thereby enhancing HOR behavior.

Introduction

Hydrogen-based fuel cell technology, a promising avenue for hydrogen energy conversion, has experienced rapid development.[1] The HOR is one of the key reactions in hydrogen–oxygen fuel cells, acting as an intermediary between the electricity and hydrogen sectors and greatly affecting the conversion efficiency. Although proton exchange membrane fuel cells (PEMFCs) hit a pinnacle in their progression, alkaline exchange membrane fuel cells (AEMFCs) have increasingly supplanted PEMFCs because they can utilize non-precious metal materials to drive the cathode oxygen reduction reaction (ORR).[2] Unfortunately, the kinetics of the anodic HOR decreases dramatically in alkaline media, dropping at least two orders of magnitude relative to acidic conditions, severely hampering its commercialization.[3] Based on Sabatier's principle, most active HOR electrocatalysts are positioned at the summit of the volcano diagram, characterized by a moderate binding energy for adsorbed hydrogen (H_{ads}).[4] Moreover, hydroxyl binding energy (OHBE) changes can elucidate the transformation of the HOR rate-determining step, and optimization OHBE can promote the Volmer step, which is essential for improving the HOR kinetics under alkaline electrolytes.[5] Consequently, striving to harmonize the ideal bifunctional mechanism of hydrogen binding energy (HBE) and OHBE is an effective strategy to guide the optimization of alkaline HOR electrocatalysts.[6]

Ruthenium (Ru) is regarded as the most promising candidate for replacing platinum owing to its abundant reserves, reasonable Ru–H bond strength, and more affordable price than platinum.[7] Incorporating ruthenium into nickel-based catalysts can tune the surface electronic structure of the catalyst, thereby optimizing the hydrogen binding energy (HBE) and achieving excellent HOR performance.[8] For instance, Zhang *et al.* introduced Ru into Ni-based catalysts, and revealed that the RuNi alloy could effectively reduce the HBE, thus increasing the catalytic rate of the HOR.[9] Furthermore, the adsorption of hydroxyl (OH_{ad}) also plays a crucial role in the HOR in alkaline media, as OH^- is involved in the fundamental steps.[10] Sun *et al.* confirmed that the strength of OH adsorption at the Ru/RuO_2 interface was better than that of the comparison sample through the Ru/RuO_2 heterostructure, suggesting that the enhanced OH_{ads} binding energy was

---

[a] *Guangxi Key Laboratory of Low Carbon Energy Materials, School of Chemistry and Pharmaceutical Sciences, Guangxi Normal University, Guilin 541004, China. E-mail: birdtjn@sina.com, xlyang@gxnu.edu.cn*

[b] *Saudi Arabia Basic Industries Corporation (SABIC) at King Abdullah University of Science and Technology (KAUST), Thuwal 23955-6900, Saudi Arabia. E-mail: isimjant@sabic.com*

† Electronic supplementary information (ESI) available. See DOI: **https://doi.org/10.1039/d4qi01233j**

favorable for the HOR reaction.[11] Weakening HBE and enhancing OHBE are inferred as the primary reasons for improved HOR performance. Another viable method to enhance the HOR activity is to construct an electronic metal–support interaction (EMSI) within the catalyst, which can effectively modulate the electronic structure between the metal and the support, thereby significantly improving catalytic activity. Recently, Yang *et al.* reported a Ru/Ni–NiO@C electrocatalyst constructed using a MOF-engaged replacement-pyrolysis strategy, suggesting that the strong EMSI effect between Ru and Ni–NiO could effectively improve the HOR performance.[12] Consequently, the construction of Ru-based catalysts with attenuated HBE and enhanced OHBE is of great significance for guidance of the exploitation of high-efficiency HOR catalysts.

This study employed a MOF-assisted strategy and *in situ* modified Ru on three-dimensional mesoporous carbon nanospheres to fabricate a heterogeneous catalyst (Ru/Ni–CeO_2) with high HOR activity. The optimized Ru/Ni–CeO_2 catalysts exhibited an open structure and abundant nickel defects, showcasing high activity and exceptional CO tolerance, attributed to the enhanced EMSI effect between Ru and Ni–CeO_2. Systematic catalyst characterization (EPR, UPS, and XPS *etc.*) revealed that Ni defect-induced Ru-modified Ni–CeO_2 underwent obvious charge remodeling, leading to enhanced charge transport and accelerated adsorption and desorption of active intermediates. This work provides new inspiration for building efficient and CO-resistant HOR catalysts *via* defect-engineered induced EMSI effects.

Results and discussion

Synthesis and characterization

As depicted in Fig. 1a, we put forward a MOF-engaged pyrolysis-reduction approach for manufacturing Ru-modified Ni–CeO_2 microspheres. Specifically, $Ce(NO_3)_3·6H_2O$, $Ni(NO_3)_2·6H_2O$, and H_3BTC precursors were mixed in certain proportions by hydrothermal and high-temperature pyrolysis strategies to prepare Ni–CeO_2 microspheres with abundant nickel vacancies. Afterwards, the Ru precursor ($RuCl_3$) was confined

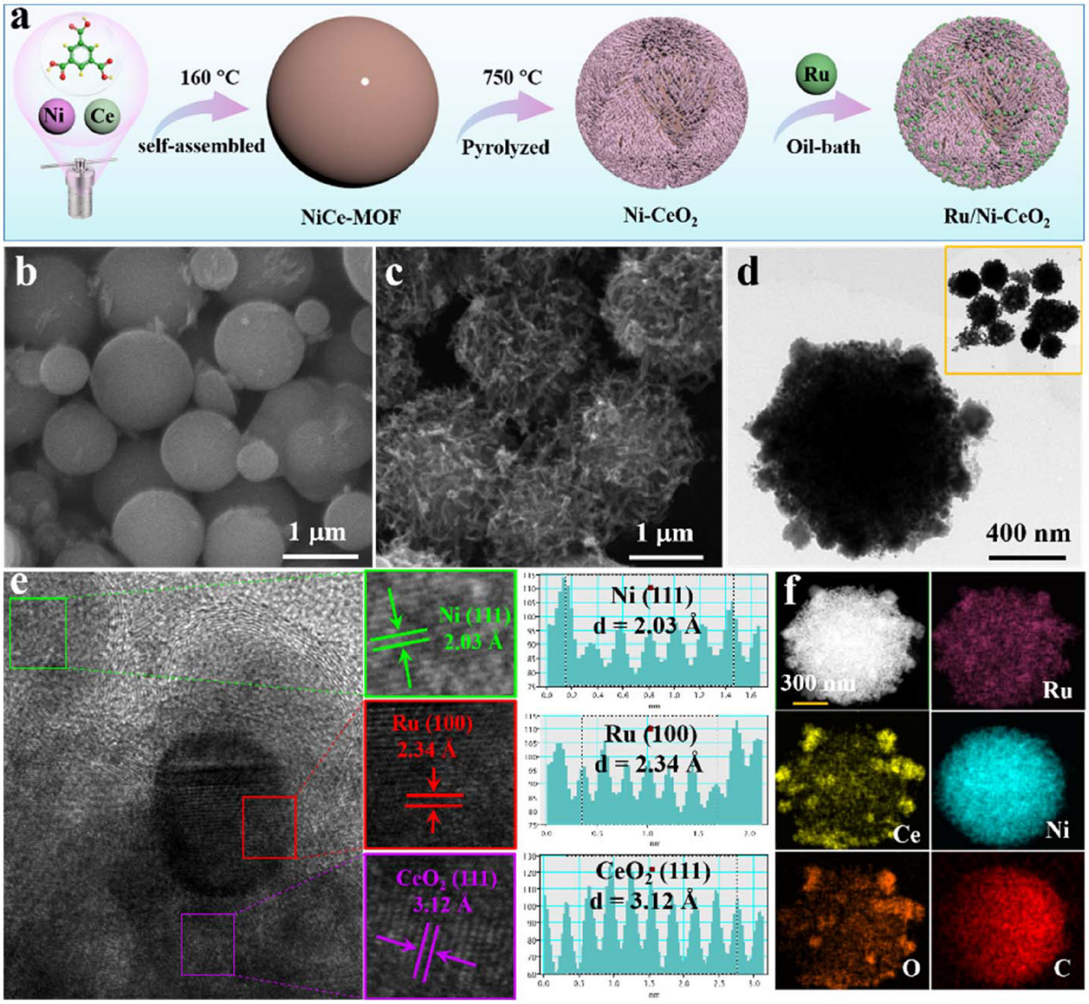

Fig. 1 (a) Preparation diagram of Ru/Ni–CeO_2 catalyst. SEM images of (b) NiCe-MOF and (c) Ru/Ni–CeO_2. (d) TEM image of Ru/Ni–CeO_2. (e) High-resolution TEM image of Ru/Ni–CeO_2. (f) Elemental mappings of Ru/Ni–CeO_2.

to the outer shells of the Ni–CeO_2 mesoporous spheres, forming a Ru/Ni–CeO_2 hybrid structure. The ample specific surface area of the finely spherical structure facilitated Ru dispersion, exposing more active sites.[13] Correspondingly, Ru/Ni and Ru/CeO_2 were prepared employing a similar approach. Scanning electron microscopy (SEM) and transmission electron microscopy (TEM) were performed to explore the morphology of the catalyst. As shown in Fig. 1b, NiCe-MOF was dispersed spherically with a smooth surface. After high-temperature annealing, smooth spherical surfaces transformed into a nanonetwork structure (Fig. 1c). Furthermore, TEM observation verified that the morphology was well inherited after modifying Ru onto Ni–CeO_2 (Fig. 1d). High-resolution TEM (HRTEM) image examination (Fig. 1e) exhibited lattice fringes for the Ru/Ni–CeO_2 microspheres of 2.03, 2.34 and 3.12 Å, representing the (111) plane of Ni, the (100) plane of Ru, and the (111) plane of CeO_2, respectively.[14] The coexistence of Ni, Ru, and CeO_2 components confirmed the successful fabrication of Ru/Ni–CeO_2 catalysts. Elemental mapping analysis presented in Fig. 1f verified the uniform distribution of Ru, Ce, Ni, O, and C elements throughout the Ru/Ni–CeO_2 microsphere structure.

XRD analysis was conducted to examine the crystal structure of the catalyst. As depicted in Fig. 2a, the diffraction peaks of Ru/Ni–CeO_2 matched with cubic phase CeO_2 (JCPDS: 78-0694) and cubic phase Ni (JCPDS: 87-0712), respectively. Similarly, Ru/CeO_2 and Ru/Ni exhibited matching peaks with cubic CeO_2 and cubic Ni (Fig. S1†), confirming the successful formation of the catalysts. However, no significant Ru diffraction peaks were observed in the XRD patterns, probably owing to the amorphous state of Ru or the minimal Ru content.[15] Furthermore, the electron paramagnetic resonance (EPR) test was applied to verify the existence of nickel vacancies. Apparently, almost symmetrical EPR signals around $g = 2.26$ were obtained in Ru/Ni–CeO_2 and Ru/Ni, while they disappeared in Ru/CeO_2 (Fig. 2b), which implied that there were Ni vacancies in Ru/Ni–CeO_2 and Ru/Ni that trapped unpaired electrons.[16] Additionally, the nickel vacancies were investigated at different calcination temperatures and varying Ru content samples (Fig. S2†). Identical EPR signals were found in these samples, indicating the presence of Ni vacancies. The Ru/Ni–CeO_2 calcinated at 700 °C with a Ru content of 3.75 wt% exhibited a more pronounced EPR signal, suggesting a greater nickel vacancy concentration. The rich Ni vacancies in Ru/Ni–CeO_2 can enhance the concentration of charge carriers and the synergistic effect between the components, promoting the adsorption and desorption of intermediates.[17]

Raman spectroscopy was employed to assess the nanomaterials' graphitization degree and structural defects.[18] Typically, broad D- (~1345 cm^{-1}) and G- (~1597 cm^{-1}) bands reflect the disorder/edge defects and graphitization of the carbon species, respectively (Fig. 2c).[13] The I_D/I_G values of Ru/Ni–CeO_2 (0.68) were the largest compared with those of Ru/Ni (0.62) and Ru/CeO_2 (0.57), suggesting that Ru/Ni–CeO_2 harvested more edge defects, favoring the intake of diverse active sites.[19] Remarkably, the Raman spectra of Ru/Ni–CeO_2 and Ru/Ni exhibited prominent peaks around 500 cm^{-1}, but they were absent in the spectra of Ru/CeO_2. Based on previous investigations, the Raman modes at about 500 cm^{-1} were inactive in perfect single crystals; however, surface effects or the

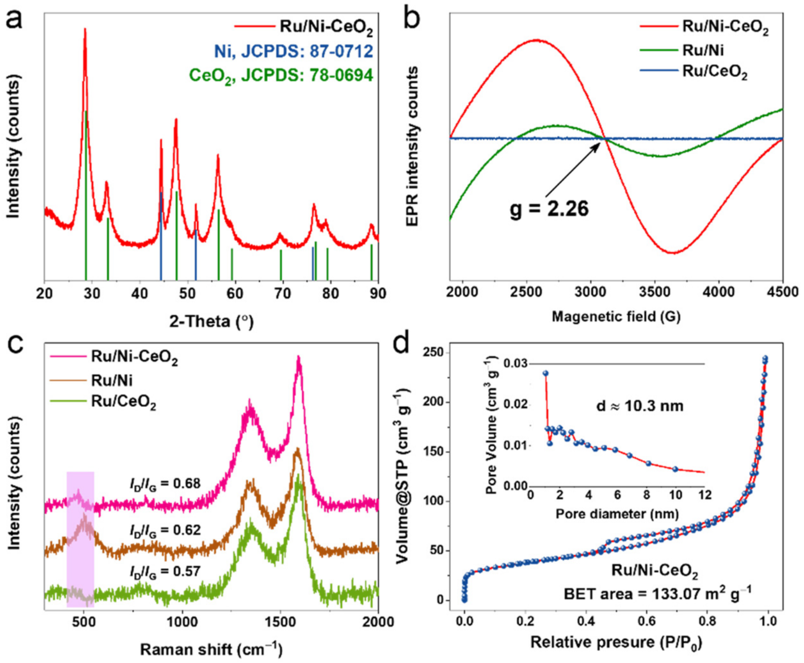

Fig. 2 (a) XRD pattern of Ru/Ni–CeO_2. (b) EPR spectra of Ru/Ni, Ru/CeO_2 and Ru/Ni–CeO_2. (c) Raman spectra of Ru/Ni, Ru/CeO_2 and Ru/Ni–CeO_2 (d) N_2 adsorption–desorption isotherms with the corresponding pore size distribution of Ru/Ni–CeO_2.

existence of vacancies made them apparent.[18] This further confirmed the appearance of a large number of intrinsic nickel vacancies in Ru/Ni–CeO_2 and Ru/Ni.[20] The abundant nickel vacancies in Ru/Ni–CeO_2 dramatically tuned the local electronic structure, thus increasing the charge-carrier concentration, accelerating charge transfer and improving the catalytic activity.[17] N_2 adsorption–desorption isotherms are displayed in Fig. 2d. Ru/Ni–CeO_2 exhibited an IV-type curve with a visible hysteresis loop, indicating that the Ru/Ni–CeO_2 nanospheres possessed a mesoporous structure with a pore size distribution of approximately 10.3 nm. Additionally, Ru/Ni–CeO_2 possessed the highest Brunauer–Emmett–Teller (BET) surface area of 133.07 $m^2\ g^{-1}$ compared to Ru/Ni (38.24 $m^2\ g^{-1}$) and Ru/CeO_2 (54.77 $m^2\ g^{-1}$), which contributed to the increased accessibility of the active site (Fig. S3†). The abundant specific surface area of the Ru/Ni–CeO_2 catalyst favored the dispersion of catalytic active sites, and the mesoporous structure was conducive to the adsorption of H_2 molecules and electron/mass transfer at heterogeneous interfaces, enhancing its catalytic performance.[21]

X-ray photoelectron spectroscopy (XPS) was employed to elucidate the surface chemical state and electronic structure of materials to identify the chemical environments of atoms. The XPS survey spectrum of Ru/Ni–CeO_2 verified the coexistence of C, O, Ni, Ce, and Ru elements (Fig. S4†). High-resolution (HR) XPS spectra of C 1s + Ru 3d (Fig. S5†) displayed deconvolution peaks at 284.0, 284.8, 286.0, 288.2, and 290.1 eV, corresponding to C=C, C–C, C–O, C=O, and O–C=O, respectively, serving as calibration benchmarks.[19,22] Meanwhile, deconvolution peaks near 281.0 and 285.1 eV represented $3d_{5/2}$ and $3d_{3/2}$ of metal Ru, respectively,[23] and the peaks at about 282.4 and 286.6 eV were $3d_{5/2}$ and $3d_{3/2}$ of RuO_2, respectively, owing to unavoidable oxidation by exposure to air.[24] Additionally, the high-resolution XPS spectra of Ru 3p further revealed the valence state of Ru. Fig. 3a depicts the deconvolution peaks at approximately 462.8 and 485.2 eV, corresponding to the $3p_{3/2}$ and $3p_{1/2}$ orbitals of metal Ru, respectively. The peaks situated around 465.9 and 488.2 eV are attributed to the $3p_{3/2}$ and $3p_{1/2}$ orbitals of RuO_2, which aligns with the literature reports.[25] Notably, the binding energy of Ru species in Ru/Ni–CeO_2 was lower than that in Ru/CeO_2, indicating electronic interaction between Ru and Ni–CeO_2.[14] In Fig. 3b, four deconvoluted peaks at 853.3, 856.9, 859.5 and 863.2 eV were associated with Ni^0, Ni^{2+}, Ni^{3+} and satellite peak species, respectively.[12] The appearance of Ni^{2+} species probably resulted from the strong interaction of unreduced Ni^{2+} with CeO_2.[26] Meanwhile, the existence of Ni^{3+} signified that Ni vacancies were successfully integrated into the lattice of Ru/Ni–CeO_2 in the annealing

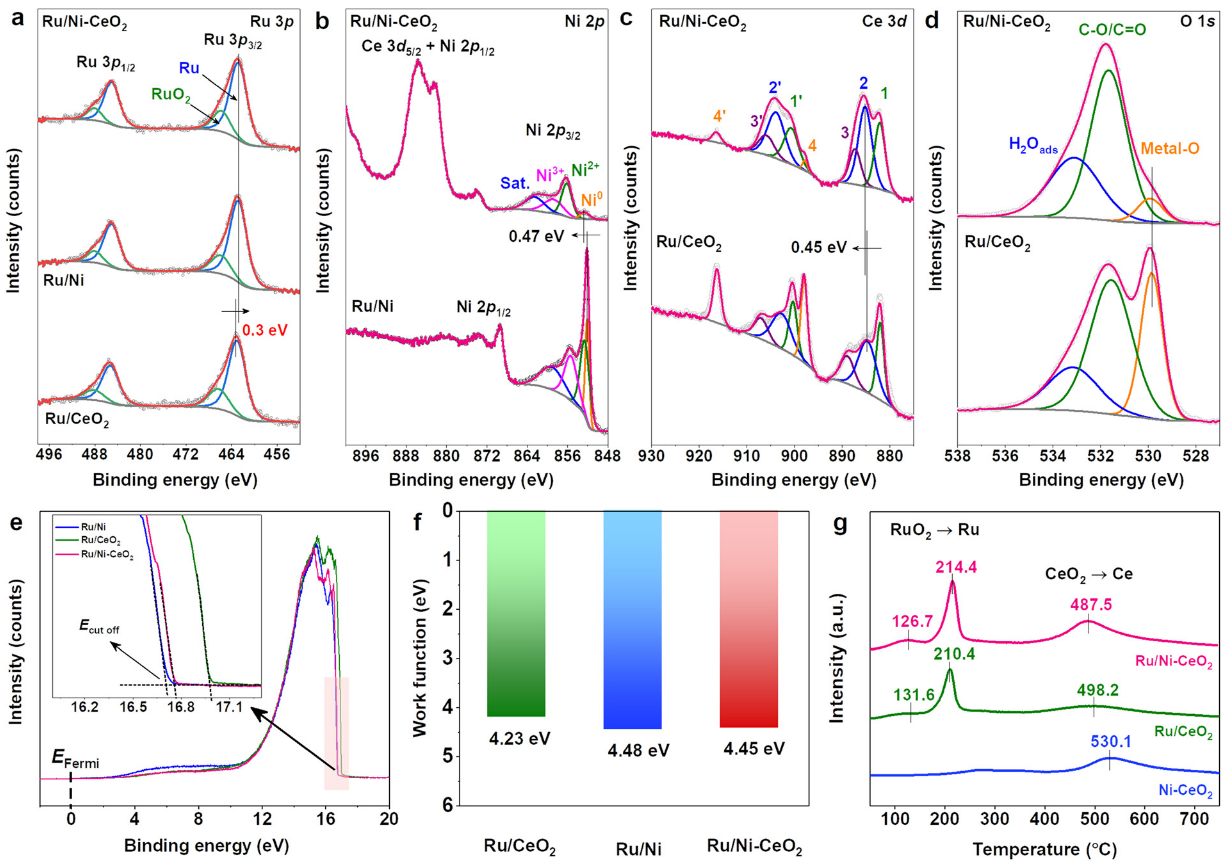

Fig. 3 High-resolution XPS spectra of (a) Ru 3p, (b) Ni 2p, (c) Ce 3d, and (d) O 1s of catalysts. (e) UPS spectra with inset partial enlargement of Ru/Ni, Ru/CeO_2 and Ru/Ni–CeO_2 catalysts and (f) corresponding work function. (g) H_2-TPR profiles of Ni–CeO_2, Ru/CeO_2 and Ru/Ni–CeO_2 catalysts.

process.[12] The oxidation of Ni^{2+} to Ni^{3+} helped to maintain the charge balance of the near-surface Ni vacancies, in line with the above Raman results.[18] Intriguingly, the Ni^0 peak in Ru/Ni–CeO_2 exhibited a positive shift of 0.47 eV compared to that in Ru/Ni, revealing a drastic electronic coupling between Ni and the other components.[26] Charge redistribution in the Ru/Ni–CeO_2 catalyst accelerated charge transfer between components, enhancing catalytic performance.[27]

As displayed in Fig. 3c, the Ce 3d spectra of the catalysts could be deconvoluted into 8 peaks. The distinctive peaks observed at 885.9 and 904.6 eV (2, 2′) were associated with Ce^{3+} ($3d^{10}4f^1$ initial electronic state), whereas the six peaks detected at 882.8, 888.1, 898.5 (1, 3, 4), and 901.4, 906.6, 917.1 eV (1′, 3′, 4′) were linked to Ce^{4+} ($3d^{10}4f^0$ initial electronic state).[28] Ce^{3+} and Ce^{4+} were identified in the Ru/Ni–CeO_2 catalyst, with Ce^{3+} likely resulting from electronic interaction between Ni^{2+} and CeO_2.[26] Apparently, the peak of Ce^{3+} in Ru/Ni–CeO_2 exhibited a positive shift of approximately 0.45 eV compared to Ru/CeO_2, indicating an electrostatic interaction between the CeO_2 and the surrounding Ni.[29] Deconvolution peaks of the O 1s XPS spectra (Fig. 3d) displayed three peaks at 529.8, 531.5, and 533.1 eV, matching metal–O, C–O/C═O, and adsorbed H_2O, respectively.[30] Additionally, the work function (WF) examined by ultraviolet photoelectron spectroscopy (UPS) can reveal the surface electronic properties of catalysts.[31] As depicted in Fig. 3e and f, the WF values of Ru/CeO_2, Ru/Ni and Ru/Ni–CeO_2 were 4.23, 4.48 and 4.45 eV, respectively. Differences in WF among catalysts corresponded to variations in surface valence states, forming unique empty d-orbitals and accelerating charge inter-transfer, consistent with XPS results.[3]

Temperature-programmed reduction (H_2-TPR) is an effective approach for probing the interfacial interactions between metals and support. As displayed in Fig. 3g, shoulder peaks were observed at 126.7 and 131.6 °C, which were induced by oxygen adsorption.[32] A peak at 214.4 °C was associated with RuO_x species strongly interacting with CeO_2.[33] The third peak at 487.5 °C was attributed to the surface oxygen reduction of CeO_2 away from Ru species. Compared to pure Ni–CeO_2 (530.1 °C), a dramatic decrease in the reduction temperature of Ru/Ni–CeO_2 (487.5 °C) was due to the loosening of Ce–O bonds strongly bound to Ru species.[32] For Ru/CeO_2 (498.2 °C), the higher reduction temperature of CeO_2 implied a stronger EMSI effect of Ru/Ni–CeO_2 compared to Ru/CeO_2. The robust EMSI effect of Ru/Ni–CeO_2 facilitated the rapid adsorption and desorption of intermediates, accelerating hydrogen oxidation in the HOR process.[12,34]

Electrochemical HOR performance

The HOR performance of the Ru/Ni–CeO_2 catalyst was assessed using rotating disk electrode (RDE) voltammetry in H_2-saturated 0.1 M KOH electrolyte *via* a standard three-electrode technique, with all electrochemical data being *iR*-corrected. Also, we provided the HOR polarization curves without IR compensation as a comparison (Fig. S6†). First, we investigated the catalytic performance under different reaction conditions and determined that the optimal HOR activity was achieved on Ru/Ni–CeO_2 with the optimal nickel vacancy annealed at 700 °C (Fig. S7†). Regarding the effect of Ru content, we observed a distinct volcano-like trend in catalytic activity, peaking at a Ru content of 3.75 wt% (Fig. S8 and Table S1†). Suboptimal performance below this level is attributed to insufficient active sites, while excessive Ru content may result in species aggregation, overwhelming the active sites. The optimal Ru content likely promotes a homogeneous distribution of Ru, thereby maximizing active site exposure, which is consistent with previous reports.[35,36]

Subsequently, the electrocatalytic performances of the synthesized Ni–CeO_2, Ru/Ni, Ru/CeO_2, and Ru/Ni–CeO_2, commercial Ru/C, and benchmark Pt/C were studied under identical conditions for comparison. As observed from the HOR polarization curves (Fig. 4a) of Ru/Ni–CeO_2, the anode current increased rapidly with increasing potential, even exceeding that for the commercial Pt/C, whereas the Ni–CeO_2 showcased a negligible current response, explaining how the EMSI effect between Ru and Ni–CeO_2 markedly accelerated the HOR reaction kinetics. As a comparative experiment, the HOR polarization curves of Ru/Ni–CeO_2 in N_2-saturated electrolyte are documented in Fig. S9,† revealing an almost inconspicuous anode current, confirming that the anode current primarily originates from H_2 oxidation. Fig. 4b presents the HOR polarization curves of Ru/Ni–CeO_2 at speed increments from 400 to 2500 rpm to obtain the relevant kinetic parameters. The Koutecky–Levich curve plotted at an overpotential of 0.1 V reveals a linear relationship between j^{-1} and $\omega^{-1/2}$ with a slope of 4.78 $cm^2\ mA^{-1}\ rpm^{1/2}$, in agreement with the theoretical value of 4.87 $cm^2\ mA^{-1}\ rpm^{1/2}$, proving the two-electron HOR process (inset in Fig. 4b).[1]

Furthermore, the kinetic current density (j_k) of the Ru/Ni–CeO_2 catalyst was calculated by measuring the Koutecky–Levich equation (Fig. 4c and e). The j_k of the Ru/Ni–CeO_2 catalyst was as high as 22.2 mA cm^{-2} at 50 mV *vs.* RHE, being 2.6-, 2.8-, 4.1-, and 16.8-fold better than those of Ru/CeO_2 (8.3 mA cm^{-2}), Ru/Ni (5.4 mA cm^{-2}), commercial Pt/C (7.8 mA cm^{-2}) and commercial Ru/C (1.3 mA cm^{-2}) catalysts, respectively. As displayed in Fig. 4d and e, we acquired the j_0 of the studied electrocatalysts by obtaining the linear fit data in the micropolarization region (−5 to 5 mV). As predicted, the j_0 of Ru/Ni–CeO_2 was calculated to be 3.27 mA cm^{-2}, and the normalized specific activity (SA) was 0.32 mA cm^{-2} (Table S2†), indicating a significant intrinsic activity of Ru/Ni–CeO_2.[37] The polarization curves of Ru/Ni–CeO_2 before and after the accelerated durability test (ADT) are shown in Fig. 4f and Fig. S10.† Remarkably, the two HOR polarization curves almost overlap after 1000 cycles, and the limiting current density exhibit only a minimal decrease after 5000 cycles. This performance is notably superior to that of commercial Pt/C. In Fig. S12,† the Ru/Ni–CeO_2-after HOR maintains its initial morphology with only minor structural collapse. Additionally, we observed that Ru, Ce^{4+} and Ni^0 signals were still present in Ru/Ni–CeO_2 after 1000 CVs (Fig. S13†). These results demonstrate that the surface structure of the catalyst was robust enough to protect the active center from alkali attack during the HOR. Moreover,

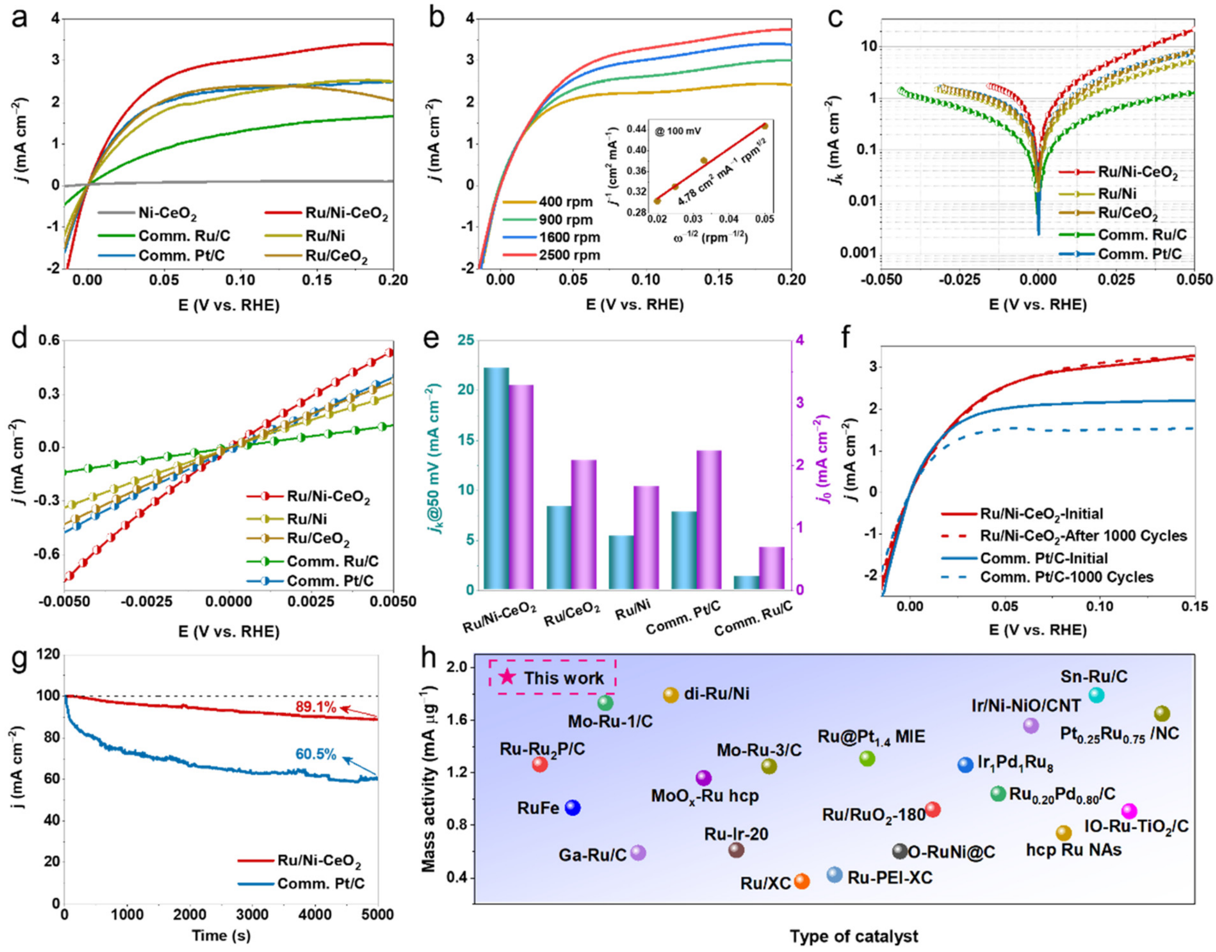

Fig. 4 (a) HOR polarization curves of catalysts in H_2-saturated 0.1 M KOH at the rotating speed of 1600 rpm. (b) Polarization curves of Ru/Ni–CeO_2 in H_2-saturated 0.1 M KOH solution at the rotating speeds varied from 400 to 2500 rpm (inset shows corresponding Koutecky–Levich plot). (c) Tafel plots. (d) Linear fitting curves in micropolarization region. (e) Summarization of j_k and j_0 of studied electrocatalysts. (f) HOR polarization curves of Ru/Ni–CeO_2 and commercial Pt/C in H_2-saturated 0.1 M KOH before and after 1000 CVs. (g) Accelerated durability test and chronoamperometry at 50 mV response of Ru/Ni–CeO_2 and commercial Pt/C. (h) Comparison og the MA with other recently reported alkaline HOR electrocatalysts.

we evaluated the ability of Ru/Ni–CeO_2 to continuously catalyze the HOR using chronoamperometry potentials ($j \approx t$) at 50 mV, which maintained the HOR reactivity throughout the test, indicating good stability (Fig. 4g). Remarkably, the mass activity (MA = 1.93 mA g_{Ru}^{-1}) of Ru/Ni–CeO_2 at 50 mV far exceeded those of most noble metal-based catalysts (Fig. 4h and Table S3†).

Both HBE and OHBE are regarded as active descriptors in the alkaline HOR process.[38] Usually, the hydrogen underpotential deposition peak (H_{upd}) is directly associated with HBE on the cyclic voltammetry curve (CV). Lower peaks in the H_{upd} region potentials reflect decreased HBE, which is more advantageous for the HOR process.[39] As illustrated in Fig. 5a, the H_{upd} peak potential of Ru/Ni–CeO_2 was more negative than those of Ru/Ni, Ru/CeO_2 and Pt/C, revealing the weaker adsorption of hydrogen on Ru sites. Considering that Ru was easily oxidized in the H adsorption/desorption potential region, it was inappropriate to calculate the ECSA by measuring the charge associated with the H_{upd} region.[40] According to previous research, CO stripping is achieved through the reaction to form OH_{ads} and CO_{ads} ($CO_{ads} + OH_{ads} \rightarrow CO_2 + H_2O$, where CO_{ads} and OH_{ads} represent the radicals adsorbed on the active sites).[41] Consequently, CO-stripping experiments were carried out to identify the ECSA values and to monitor the binding strength of *OH on the investigated catalysts. The ECSA value of Ru/Ni–CeO_2 was 62.1 $m^2\ g^{-1}$, higher than those of Ru/Ni (30.5 $m^2\ g^{-1}$), Ru/CeO_2 (19.2 $m^2\ g^{-1}$) and commercial Pt/C (35.7 $m^2\ g^{-1}$), as shown in Fig. S11 and Table S2.† The larger ECSA indicated that the more catalytic active sites could adsorb more active intermediates and accelerate the reaction speed.[42] Meanwhile, as exhibited in Fig. 5b, the CO-stripping peak of Ru/Ni–CeO_2 (0.612 V) was more negative compared to Ru/Ni (0.643 V), Ru/CeO_2 (0.741 V) and commercial Pt/C (0.731 V). This suggested that Ru/Ni–CeO_2 possessed a stronger binding affinity for OH_{ads}.

CO tolerance is a desirable characteristic for hydrogen fuel cell applications due to the primary industrial production of hydrogen coming from the reforming of hydrocarbons by

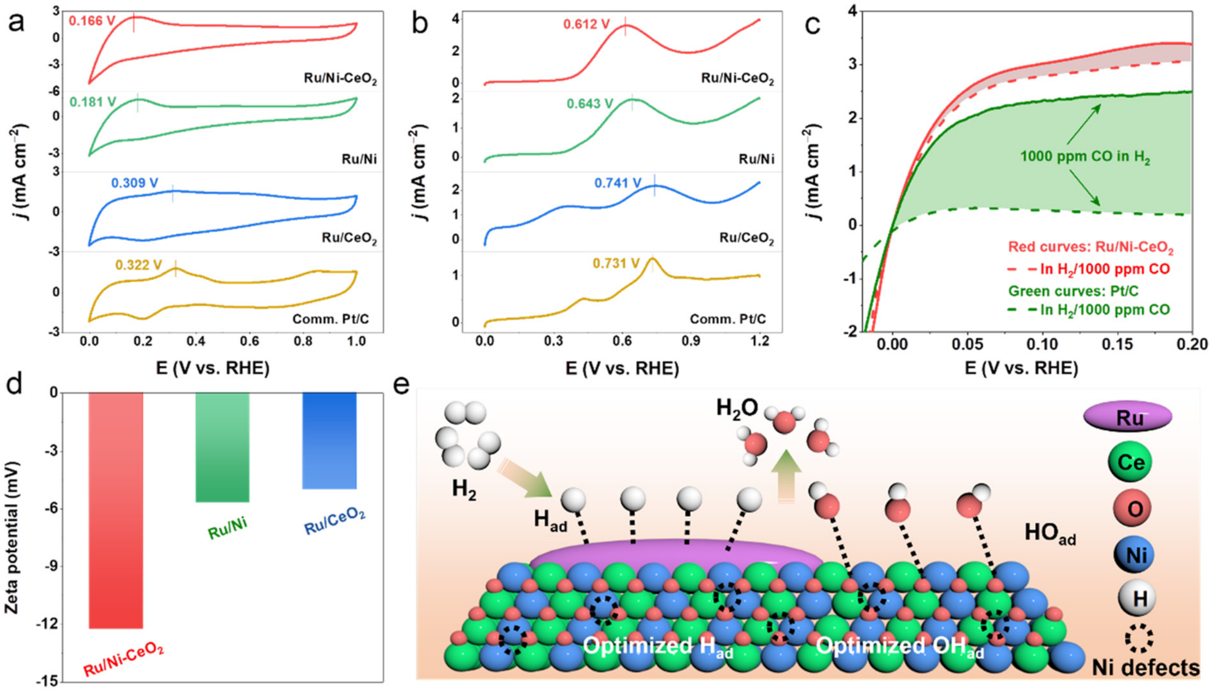

Fig. 5 (a) CV curves of Ru/Ni, Ru/CeO$_2$, Ru/Ni–CeO$_2$ and commercial Pt/C in N$_2$-saturated 0.1 M KOH. (b) CO stripping curves of Ru/Ni, Ru/CeO$_2$, Ru/Ni–CeO$_2$ and commercial Pt/C. (c) Comparison of the HOR polarization curves of Ru/Ni–CeO$_2$ and commercial Pt/C in H$_2$-saturated 0.1 M KOH containing 1000 ppm CO. (d) Zeta potential of Ru/Ni, Ru/CeO$_2$, and Ru/Ni–CeO$_2$. (e) Schematic illustration of HOR catalysis on the Ru/Ni–CeO$_2$.

natural gas.[43] In order to evaluate the CO tolerance of Ru/Ni–CeO$_2$ catalysts, the electrochemical performance was conducted in H$_2$-saturated (containing 1000 ppm CO) 0.1 M KOH. As depicted in Fig. 5c, Ru/Ni–CeO$_2$ maintained excellent HOR activity without an evident decrease, whereas the activity of the commercial Pt/C decreased dramatically, implying the impressive CO tolerance of Ru/Ni–CeO$_2$.[44] In addition, the zeta-potential (Fig. 5d) of Ru/Ni–CeO$_2$ (−12.3 mV) was more negative than those of Ru/Ni (−5.73 mV) and Ru/CeO$_2$ (−5.05 mV). More negative zeta-potentials imply stronger OHBE, consistent with the results of CO stripping experiments.[45]

Catalytic mechanism

Exploring the mechanism was essential to understanding the excellent HOR performance of Ru/Ni–CeO$_2$. The CV investigation results (Fig. 5a) showed that the HBE of Ru/Ni–CeO$_2$ was the weakest, indicating weak H binding to Ru/Ni–CeO$_2$. LSV tests showed that Ru/Ni–CeO$_2$ exhibited the best HOR activity, while Ni–CeO$_2$ was nearly inactive (Fig. 4a), confirming that Ru served as the active site for hydrogen adsorption (H$_{ads}$). Additionally, the CO-oxidation peak of Ru/Ni–CeO$_2$ was the most negative, implying that Ru/Ni–CeO$_2$ had the strongest bonding with OH$^-$ based on the correlation between the CO stripping potential and the adsorption strength of OH$^-$ (Fig. 5b). The augmented OH$_{ads}$ adsorption behavior and surface structure containing Ni vacancies would boost the trapping of OH$_{ads}$ species on the surface of Ni–CeO$_2$, thus accelerating the Volmer step in the alkaline HOR process through a bifunctional mechanism at the boundary between the Ru and Ni–CeO$_2$ components, involving the adsorption of H$_{ad}$ compounds on Ru and that of OH$_{ad}$ on Ni–CeO$_2$.[46,47] Consequently, we proposed a bifunctional mechanism for Ru/Ni–CeO$_2$ by combining CV and CO stripping analysis (Fig. 5e). Specifically, Ru served as a favorable adsorption site for H$_{ad}$, and H$_2$ molecules first dissociated and adsorbed on the Ru metal surface to form H$_{ad}$ (denoted as Ru–H$_{ad}$). Meanwhile, Ni–CeO$_2$ became an adsorption site for OH to form OH$_{ad}$ (marked as Ni–CeO$_2$–OH$_{ad}$), and the last two intermediates (H$_{ad}$ and OH$_{ad}$) reacted to form H$_2$O. It is observed that the synergistic adsorption of H and OH$^-$ species between Ru and Ni–CeO$_2$ in the Ni vacancy-rich Ru/Ni–CeO$_2$ heterogeneity promoted HOR kinetics, thus exhibiting remarkable HOR activity.[48]

Conclusion

Overall, we proved the availability of the Ru/Ni–CeO$_2$ microsphere structure as a highly efficient electrocatalyst for the hydrogen oxidation reaction (HOR) in alkaline environments. The as-prepared Ru/Ni–CeO$_2$ showcased admirable HOR performance with a dramatically improved exchange current density and electrochemical surface area, outperforming comparable catalysts and even commercial Pt/C. The remarkable characteristics of Ru/Ni–CeO$_2$ were ascribed to the EMSI between Ru and Ni–CeO$_2$ components, resulting in a redistribution of the surface charge density. The charge redistribution was evidenced to optimize the adsorption of hydrogen (H) and hydroxyl (OH) species, leading to enhancement of the HOR kinetics. Furthermore, Ru/Ni–CeO_2 exhibited remarkable long-term stability and CO tolerance. This work offers new insights into advanced catalyst design for the efficient exploitation of hydrogen fuels, benefiting the development of a zero-carbon economy.

Author contributions

Shuqing Zhou: Writing – original draft, methodology. Yi Liu: Methodology, writing – original draft. Lianrui Cheng: Validation, investigation. Tayirjan Taylor Isimjan: Writing – review & editing. Jianniao Tian: Writing – review & editing, supervision. Xiulin Yang: Writing – review & editing, supervision.

Data availability

The data supporting this article have been included as part of the ESI.†

Conflicts of interest

There are no conflicts to declare.

Acknowledgements

This work has been supported by the National Natural Science Foundation of China (No. 52363028, 21965005), the Natural Science Foundation of Guangxi Province (2021GXNSFAA076001, 2018GXNSFAA294077), Guangxi Technology Base and Talent Subject (GUIKE AD23023004, GUIKE AD20297039), and the Innovation Project of Guangxi Graduate Education (YCSW2024228).

References

1 Y. Duan, X. L. Zhang, F. Y. Gao, Y. Kong, Y. Duan, X. T. Yang, X. X. Yu, Y. R. Wang, S. Qin, Z. Chen, R. Wu, P. P. Yang, X. S. Zheng, J. F. Zhu, M. R. Gao, T. B. Lu, Z. Y. Yu and S. H. Yu, Interfacial engineering of Ni/V_2O_3 heterostructure catalyst for boosting hydrogen oxidation reaction in alkaline electrolytes, *Angew. Chem., Int. Ed.*, 2023, **62**, e202217275.

2 Y. Kwon, D. S. Hong, J. H. Jang, M. Kim, S. Oh, D. H. Song, J. Lim, S. J. Yoo and E. A. Cho, A Ni-MoO_x composite catalyst for the hydrogen oxidation reaction in anion exchange membrane fuel cell, *Appl. Catal., B*, 2023, **332**, 122740.

3 L. Su, X. Fan, Y. Jin, H. Cong and W. Luo, Hydroxyl-binding energy-induced kinetic gap narrowing between acidic and alkaline hydrogen oxidation reaction on intermetallic Ru_3Sn_7 catalyst, *Small*, 2023, **19**, 2207603.

4 M. T. M. Koper, A basic solution, *Nat. Chem.*, 2013, **5**, 255–256.

5 I. T. McCrum and M. T. M. Koper, The role of adsorbed hydroxide in hydrogen evolution reaction kinetics on modified platinum, *Nat. Energy*, 2020, **5**, 891–899.

6 L. X. Su, Y. M. Jin, X. R. Fan, Z. Y. Liu and W. Luo, pH-Dependent binding energy-induced inflection-point behaviors for pH-universal hydrogen oxidation reaction, *Sci. China: Chem.*, 2023, **66**, 3262–3268.

7 X. Yang, B. Ouyang, P. Shen, Y. Sun, Y. Yang, Y. Gao, E. Kan, C. Li, K. Xu and Y. Xie, Ru colloidosome catalysts for the hydrogen oxidation reaction in alkaline media, *J. Am. Chem. Soc.*, 2022, **144**, 11138–11147.

8 Y. Dong, Q. Sun, C. Zhan, J. Zhang, H. Yang, T. Cheng, Y. Xu, Z. Hu, C. W. Pao, H. Geng and X. Huang, Lattice and surface engineering of ruthenium nanostructures for enhanced hydrogen oxidation catalysis, *Adv. Funct. Mater.*, 2022, **33**, 2210328.

9 X. Zhang, Z. Li, X. Sun, L. Wei, H. Niu, S. Chen, Q. Chen, C. Wang and F. Zheng, Regulating the surface electronic structure of RuNi alloys for boosting alkaline hydrogen oxidation electrocatalysis, *ACS Mater. Lett.*, 2022, **4**, 2097–2105.

10 S. Qin, Y. Duan, X.-L. Zhang, L.-R. Zheng, F.-Y. Gao, P.-P. Yang, Z.-Z. Niu, R. Liu, Y. Yang, X.-S. Zheng, J.-F. Zhu and M.-R. Gao, Ternary nickel–tungsten–copper alloy rivals platinum for catalyzing alkaline hydrogen oxidation, *Nat. Commun.*, 2021, **12**, 2686.

11 X. Zhang, L. Xia, G. Zhao, B. Zhang, Y. Chen, J. Chen, M. Gao, Y. Jiang, Y. Liu, H. Pan and W. Sun, Fast and durable alkaline hydrogen oxidation reaction at the electron-deficient ruthenium–ruthenium oxide interface, *Adv. Mater.*, 2023, **35**, 2208821.

12 Y. Yang, Y. Huang, S. Zhou, Y. Liu, L. Shi, T. T. Isimjan and X. Yang, Delicate surface vacancies engineering of Ru doped MOF-derived Ni-NiO@C hollow microsphere superstructure to achieve outstanding hydrogen oxidation performance, *J. Energy Chem.*, 2022, **72**, 395–404.

13 M. Guo, Z. Huang, Y. Qu, L. Wang, H. Li, T. T. Isimjan and X. Yang, Synergistic effect and nanostructure engineering of three-dimensionally hollow mesoporous spherical Cu_3P/TiO_2 in aqueous/flexible Zn–air batteries, *Appl. Catal., B*, 2023, **320**, 121991.

14 Y. Liu, L. Cheng, Y. Huang, Y. Yang, X. Rao, S. Zhou, T. T. Isimjan and X. Yang, Electronic modulation and mechanistic study of Ru-decorated porous Cu-rich cuprous oxide for robust alkaline hydrogen oxidation and evolution reactions, *ChemSusChem*, 2023, **16**, e202202113.

15 D. D. Tuan and K.-Y. A. Lin, Ruthenium supported on ZIF-67 as an enhanced catalyst for hydrogen generation from hydrolysis of sodium borohydride, *Chem. Eng. J.*, 2018, **351**, 48–55.

16 Z. Zhou, Y. Kong, H. Tan, Q. Huang, C. Wang, Z. Pei, H. Wang, Y. Liu, Y. Wang, S. Li, X. Liao, W. Yan and

S. Zhao, Cation-vacancy-enriched nickel phosphide for efficient electrosynthesis of hydrogen peroxides, *Adv. Mater.*, 2022, **34**, 2106541.

17 X. Lei, J. Wang, T. Wang, X. Wang, X. Xie, H. Huang, D. Li and Z. Ao, Toluene decomposition by non-thermal plasma assisted CoO_x–γ-Al_2O_3: The relative contributions of specific energy input of plasma, Co^{3+} and oxygen vacancy, *J. Hazard. Mater.*, 2023, **456**, 131613.

18 A. Tang, C. Wan, X. Hu and X. Ju, Metal-organic framework-derived Ni/ZnO nano-sponges with delicate surface vacancies as anode materials for high-performance supercapacitors, *Nano Res.*, 2021, **14**, 4063–4072.

19 J. Li, Y. Kang, Z. Lei and P. Liu, Well-controlled 3D flower-like $CoP_3/CeO_2/C$ heterostructures as bifunctional oxygen electrocatalysts for rechargeable Zn–air batteries, *Appl. Catal., B*, 2023, **321**, 122029.

20 N. Mironova-Ulmane, A. Kuzmin, I. Steins, J. Grabis, I. Sildos and M. Pärs, Raman scattering in nanosized nickel oxide NiO, *J. Phys.: Conf. Ser.*, 2007, **93**, 012039.

21 X. Zhao, X. Yu, S. Xin, S. Chen, C. Bao, W. Xu, J. Xue, B. Hui, J. Zhang, X. She and D. Yang, Enhanced oxygen reduction reaction for Zn–air battery at defective carbon fibers derived from seaweed polysaccharide, *Appl. Catal., B*, 2022, **301**, 120785.

22 Y. Liu, Y. Huang, S. Zhou, Y. Yang, L. Cheng, T. T. Isimjan and X. Yang, Synergistic regulation of Pt clusters on porous support by Mo and P for robust bifunctional hydrogen electrocatalysis, *Inorg. Chem.*, 2023, **62**, 8719–8728.

23 Y. Liu, X. Li, Q. Zhang, W. Li, Y. Xie, H. Liu, L. Shang, Z. Liu, Z. Chen, L. Gu, Z. Tang, T. Zhang and S. Lu, A general route to prepare low-ruthenium-content bimetallic electrocatalysts for pH-universal hydrogen evolution reaction by using carbon quantum dots, *Angew. Chem., Int. Ed.*, 2020, **59**, 1718–1726.

24 C. Li, H. Jang, S. Liu, M. G. Kim, L. Hou, X. Liu and J. Cho, P and Mo dual Doped Ru ultrasmall nanoclusters embedded in P-doped porous carbon toward efficient hydrogen evolution reaction, *Adv. Energy Mater.*, 2022, **12**, 2200029.

25 X. Mu, X. Zhang, Z. Chen, Y. Gao, M. Yu, D. Chen, H. Pan, S. Liu, D. Wang and S. Mu, Constructing symmetry-mismatched $Ru_xFe_{3-x}O_4$ heterointerface-supported Ru clusters for efficient hydrogen evolution and oxidation reactions, *Nano Lett.*, 2024, **24**, 1015–1023.

26 H. Liu, Y. Zhang, S. Liu, S. Li and G. Liu, Ni-CeO_2 nanocomposite with enhanced metal-support interaction for effective ammonia decomposition to hydrogen, *Chem. Eng. J.*, 2023, **473**, 145371.

27 T. Chen, F. Wang, S. Cao, Y. Bai, S. Zheng, W. Li, S. Zhang, S. X. Hu and H. Pang, In situ synthesis of MOF-74 family for high areal energy density of aqueous nickel–zinc batteries, *Adv. Mater.*, 2022, **34**, 2201779.

28 Y. Wang, Z. Li, X. Zheng, R. Wu, J. Song, Y. Chen, X. Cao, Y. Wang and Y. Nie, Renovating phase constitution and construction of Pt nanocubes for electrocatalysis of methanol oxidation via a solvothermal-induced strong metal–support interaction, *Appl. Catal., B*, 2023, **325**, 122383.

29 L. Shi, K. Zhu, Y. Yang, Y. Liu, S. Xu, T. T. Isimjan and X. Yang, Oxygen-vacancy-rich Ru-clusters decorated Co/Ce oxides modifying ZIF-67 nanocubes as a high-efficient catalyst for $NaBH_4$ hydrolysis, *Int. J. Hydrogen Energy*, 2022, **47**, 37840–37849.

30 R. Zhang, L. Hu, S. Bao, R. Li, L. Gao, R. Li and Q. Chen, Surface polarization enhancement: High catalytic performance of $Cu/CuO_x/C$ nanocomposites derived from Cu-BTC for CO oxidation, *J. Mater. Chem. A*, 2016, **4**, 8412–8420.

31 W. Ren, X. Tan, C. Jia, A. Krammer, Q. Sun, J. Qu, S. C. Smith, A. Schueler, X. Hu and C. Zhao, Electronic regulation of nickel single atoms by confined nickel nanoparticles for energy-efficient CO_2 electroreduction, *Angew. Chem., Int. Ed.*, 2022, **61**, e202203335.

32 H. Huang, Q. Dai and X. Wang, Morphology effect of Ru/CeO_2 catalysts for the catalytic combustion of chlorobenzene, *Appl. Catal., B*, 2014, **158–159**, 96–105.

33 Y. Guo, S. Mei, K. Yuan, D.-J. Wang, H.-C. Liu, C.-H. Yan and Y.-W. Zhang, Low-temperature CO_2 methanation over CeO_2-supported ru single atoms, nanoclusters, and nanoparticles competitively tuned by strong metal–support interactions and H-spillover effect, *ACS Catal.*, 2018, **8**, 6203–6215.

34 S. Zhou, Q. Yang, Y. Liu, L. Cheng, T. T. Isimjan, J. Tian and X. Yang, Electronic metal–support interactions for defect-induced Ru/Co-Sm_2O_3 mesosphere to achieve efficient $NaBH_4$ hydrolysis activity, *J. Catal.*, 2024, **433**, 115491.

35 Y. Liu, L. Cheng, S. Zhou, Y. Yang, C. Niu, T. T. Isimjan, B. Wang and X. Yang, Revealing interfacial charge redistribution of homologous Ru-RuS_2 heterostructure toward robust hydrogen oxidation reaction, *J. Energy Chem.*, 2024, **94**, 332–339.

36 C. Jin, Y. Liao, A. Zhang, S. Zhao, R. Wang, J. Li and H. Tang, Low-Pt anodes with gradient molybdenum isomorphism for high performance and anti-CO poisoning PEMFCs, *Nano Energy*, 2024, **122**, 109305.

37 M. Fang, Y. Ji, S. Geng, J. Su, Y. Li, Q. Shao and J. Lu, Metastable metal–alloy interface in RuNi nanoplates boosts highly efficient hydrogen electrocatalysis, *ACS Appl. Nano Mater.*, 2022, **5**, 17496–17502.

38 Y. Duan, Z.-Y. Yu, L. Yang, L.-R. Zheng, C.-T. Zhang, X.-T. Yang, F.-Y. Gao, X.-L. Zhang, X. Yu, R. Liu, H.-H. Ding, C. Gu, X.-S. Zheng, L. Shi, J. Jiang, J.-F. Zhu, M.-R. Gao and S.-H. Yu, Bimetallic nickel–molybdenum/tungsten nanoalloys for high-efficiency hydrogen oxidation catalysis in alkaline electrolytes, *Nat. Commun.*, 2020, **11**, 4789.

39 C. Yang, Y. Li, J. Yue, H. Cong and W. Luo, Promoting water formation in sulphate-functionalized Ru for efficient hydrogen oxidation reaction under alkaline electrolytes, *Chem. Sci.*, 2023, **14**, 6289–6294.

40 B. Qin, H. Yu, X. Gao, D. Yao, X. Sun, W. Song, B. Yi and Z. Shao, Ultrathin IrRu nanowire networks with high performance and durability for the hydrogen oxidation reaction in alkaline anion exchange membrane fuel cells, *J. Mater. Chem. A*, 2018, **6**, 20374–20382.

41 L. Chen, L. Lu, H. Zhu, Y. Chen, Y. Huang, Y. Li and L. Wang, Improved ethanol electrooxidation performance by shortening Pd–Ni active site distance in Pd–Ni–P nanocatalysts, *Nat. Commun.*, 2017, **8**, 14136.

42 S. Lyu, C. Guo, J. Wang, Z. Li, B. Yang, L. Lei, L. Wang, J. Xiao, T. Zhang and Y. Hou, Exceptional catalytic activity of oxygen evolution reaction via two-dimensional graphene multilayer confined metal–organic frameworks, *Nat. Commun.*, 2022, **13**, 6171.

43 G. S. D. A. Tryk, H. Yano, J. Inukai, H. Uchida, A. Iiyama, M. Matsumoto, H. Tanida, M. Arao and H. Imai, Recent progress in the understanding of the electrocatalysis of the CO-tolerant hydrogen oxidation reaction in polymer electrolyte fuel cells, *ECS Trans.*, 2018, **85**, 41–46.

44 Y. Li, C. Yang, J. Yue, H. Cong and W. Luo, Polymorphism-interface-induced work function regulating on Ru nanocatalyst for enhanced alkaline hydrogen oxidation reaction, *Adv. Funct. Mater.*, 2023, **33**, 2211586.

45 L. Su, Y. Jin, D. Gong, X. Ge, W. Zhang, X. Fan and W. Luo, The role of discrepant reactive intermediates on Ru-Ru_2P heterostructure for pH-universal hydrogen oxidation reaction, *Angew. Chem., Int. Ed.*, 2023, **62**, e202215585.

46 F. Yang, X. Bao, P. Li, X. Wang, G. Cheng, S. Chen and W. Luo, Boosting hydrogen oxidation activity of Ni in alkaline media through oxygen-vacancy-rich CeO_2/Ni heterostructures, *Angew. Chem., Int. Ed.*, 2019, **58**, 14179–14183.

47 D. Strmcnik, M. Uchimura, C. Wang, R. Subbaraman, N. Danilovic, D. van der Vliet, A. P. Paulikas, V. R. Stamenkovic and N. M. Markovic, Improving the hydrogen oxidation reaction rate by promotion of hydroxyl adsorption, *Nat. Chem.*, 2013, **5**, 300–306.

48 Y. Men, X. Su, P. Li, Y. Tan, C. Ge, S. Jia, L. Li, J. Wang, G. Cheng, L. Zhuang, S. Chen and W. Luo, Oxygen-inserted top-surface layers of ni for boosting alkaline hydrogen oxidation electrocatalysis, *J. Am. Chem. Soc.*, 2022, **144**, 12661–12672.